

Article

Mountain Waves in High Resolution Forecast Models: Automated Diagnostics of Wave Severity and Impact on Surface Winds

Peter Sheridan *, Simon Vosper and Philip Brown

Met Office, FitzRoy Rd., Exeter EX1 3PB, UK; simon.vosper@metoffice.gov.uk (S.V.); phil.brown@metoffice.gov.uk (P.B.)

* Correspondence: peter.sheridan@metoffice.gov.uk

Academic Editor: Vanda Grubišić

Received: 30 November 2016; Accepted: 16 January 2017; Published: 23 January 2017

Abstract: An automated method producing a diagnostic of the severity of lee waves and their impacts on surface winds as represented in output from a high resolution linear numerical model (3D velocities over mountains (3DVOM)) covering several areas of the U.K. is discussed. Lee waves involving turbulent rotor activity or downslope windstorms represent a hazard to aviation and ground transport, and summary information of this kind is highly valuable as an efficient ‘heads-up’ for forecasters, for automated products or to feed into impact models. Automated diagnosis of lee wave surface effects presents a particular challenge due to the complexity of turbulent zones in the lee of irregular terrain. The method proposed quantifies modelled wind perturbations relative to those that would occur in the absence of lee waves for a given background wind, and diagnoses using it are found to be quite consistent between cases and for different ranges of U.K. hills. A recent upgrade of the operational U.K. limited area model, the U.K. Variable Resolution Model (UKV) used for general forecasting at the Met Office means that it now resolves lee waves, and its performance is here demonstrated using comparisons with aircraft- and surface-based observations and the linear model. In the future, automated diagnostics may be adapted to use its output to routinely produce contiguous mesoscale maps of lee wave activity and surface impacts over the whole U.K.

Keywords: lee waves; high resolution; numerical weather prediction; turbulence; rotor; aviation; diagnostic; automation

1. Introduction

Mountain waves, induced by stable tropospheric flow over terrain, are a well-known source of aviation hazards, such as strong up- and down-drafts, downslope windstorms [1–4], clear air turbulence (CAT) associated with tropospheric wave breaking [5–10], low-level turbulence and ‘rotors’ associated with wave-induced boundary layer separation [11–17] and hydraulic jump-like flows [12,18], as well as hazards to surface transport [19], such as very strong or gusty winds [20].

Trapped lee waves (‘lee waves’ herein), in which wave energy is ducted close to the surface [13,21,22], impact the strength and turbulence of boundary-layer flow and are of particular importance for ground and low-level air operations. Though the term is often used for any dramatic manifestations of low-level wave-induced turbulence and wind variability, ‘rotors’ are usually described in terms of a tubular recirculation vortex in the lee of a quasi-two-dimensional (2D) ridge. This forms when lee waves induce an adverse pressure gradient near the surface of sufficient magnitude to reverse the flow there, resulting in boundary layer separation beneath the lee wave crest, which lofts vorticity away from the surface [11,13,14,23–26]. While this concept was often confirmed in idealised situations using physical [26] or computational/analytical [12,13] models (including one described in another submission to this special issue [27]), more often, turbulent zones downwind of complex

terrain have a likewise complex structure [17,28–31], so that the near-surface flow field is perhaps more usefully described in terms of wave-induced flow perturbation. In this paper, though the term ‘rotor’ is much used, it is generally considered in a practical sense to mean wave-induced flow perturbation consistent in magnitude with rotor formation; we soften the terminology where appropriate to reflect this (‘rotor-like’, ‘rotor activity’, use of quotation marks, etc.). Further, above the surface, lee wave patterns in vertical velocity over complex terrain can be difficult to discern from variations in vertical velocity (w) caused directly by displacement over the terrain, so that a measure of the wave-induced component of vertical flow perturbation can also be a useful way to view lee waves. It has been shown that, for lee waves of a given amplitude, rotors form more easily when near-surface winds are weaker [13,14], so that wave amplitude alone is not a reliable predictor of large near-surface wind perturbations, such as rotor formation.

A number of approaches exist that simulate gravity waves and their effects in forecast models. These include gravity wave drag parametrisation schemes in global Numerical Weather Prediction (NWP) models [32], diagnostics from which are also employed to produce forecasts of en-route clear air turbulence (CAT) for aviation [33–35]. Orographic drag parametrizations typically do not, however, contain a representation of trapped lee waves and, thus, of course, provide no forecast of associated low-level turbulence, although recent research demonstrates a convincing link between high lee-wave drag and rotor formation [36]. Informal forecasts of lee wave activity are produced by the sailplane (or ‘glider’) flying community, who exploit lee waves for lift, using limited area model (LAM) simulations run at high resolution nested into publicly-available global NWP forecasts (Regional Atmospheric Soaring Prediction system (RASP), H. Ford, Met Office, personal communication). Numerical modelling is used at the Hong Kong Observatory (HKO) to predict lee waves or low level turbulence, including the high resolution aviation model (AVM) [37,38] and other approaches [39,40]. A nested high resolution model based on non-linear dynamical equations has also been used for forecasting wind shear and turbulence at Norwegian airports [41].

At the Met Office, the 3D velocities over mountains (3DVOM) model is used for lee wave forecasting in support of low-level aviation operations. 3DVOM is a linear model that assumes a horizontally-uniform background flow derived from a single profile from the Met Office global forecast model (described in more detail in Section 2) The vertical and horizontal wind fields produced by the model tend to verify reasonably well in the areas of moderate terrain where it is typically used [42–44], where its linear dynamics assumptions are generally appropriate. The model’s simplified approach renders it computationally efficient. An adapted version of the model has been used in conjunction with larger terrain, including for mission planning during the Terrain-Induced Rotor Experiment (T-REX) field campaign, alongside another the linear model and the Naval Research Laboratory (NRL) Coupled Ocean/Atmosphere Mesoscale Prediction System (COAMPS) at comparable resolutions [45]. 3DVOM is preferred over simpler lee wave prediction schemes [22,46], which are designed to post-process profiles from coarse resolution operational NWP data. A regime diagram for the prediction of rotors due to lee waves on a low-level temperature inversion [12] provides the basis for another forecasting tool used at the Met Office. This is useful in the Falkland Islands, where lee waves are linked to the presence of such inversions, but may not generally be used to predict rotors over the U.K., where lee waves are usually the result of more gradual vertical variation of temperature and wind with height [14].

The 3DVOM model employs a horizontal grid resolution of 1 km. For efficient use of forecasters’ time, simple automated diagnostics from the model fields are desirable as ‘headline’ summaries of wave activity. Following recent upgrades to the Met Office Unified Model (MetUM, the principal NWP model used at the Met Office as a ‘seamless’ system for global and regional weather and climate prediction), an explicit simulation of lee waves is now available in a 1.5-km resolution U.K. configuration, the U.K. Variable Resolution Model (UKV). The relative sophistication of this core NWP model, the routine general validation applied to it and its full U.K. coverage suggest it as a successor to 3DVOM, once its lee wave forecasting capability is assessed. The adaptation for use with UKV

of automated lee wave diagnostics developed for 3DVOM will thus likely be desirable in the future, as well. The latter will be challenging since flows in 3DVOM, a dry, linear model forced by simple boundary conditions, are inherently simpler than those in UKV, whose suite of parametrisations and ability to support realistic convection, moist physics and non-linear processes mean that automated post-processing methods must discern lee waves from other sources of vertical motion and near-surface flow perturbation. The efforts here are likely to be relevant to other forecast centres, whose operational models are going through equivalent evolution [37,38,47–49].

In this paper, diagnostics for forecasting lee wave and rotor-like activity based on 3DVOM are explained. Furthermore, forecast output from UKV is compared against recent aircraft measurements of vertical velocities by the Facility for Airborne Atmospheric Measurement (FAAM) BAe-146 aircraft, sampling lee waves over the Scottish mountains. The challenges associated with the adaptation of the diagnostics for use with UKV are also discussed. Section 2 details the methods used to acquire observations and model forecasts. The development of lee wave and rotor activity diagnostics and verification of UKV model data against aircraft measurements are described in Section 3 and discussed further in Section 4. Conclusions are summarised in Section 5.

2. Materials and Methods

2.1. The Met Office Unified Model and UKV Configuration

The Met Office Unified Model (MetUM) is the NWP model routinely used to produce forecasts at the Met Office. The vertical profiles used to drive the 3DVOM model are sourced from the global configuration of the model. The global configuration is also used to provide lateral boundary conditions (LBCs) for the UKV configuration, which operates with a stretched grid, with a grid length of 4 km at its outer edge gradually decreasing to 1.5-km resolution by the time it reaches a central region covering the British Isles. UKV operates with a suite of physical parametrisations tailored for this resolution. More details on the UKV configuration are given elsewhere [50]. More recently, the dynamic core of the model was replaced with a new version, ENDGame (Even Newer Dynamics for General atmospheric modelling of the environment) [51]. This core supports short wavelength gravity wave activity more readily than the previous dynamical core, which required the use of computationally-expensive (due to numerical instability issues) dynamics settings in order to simulate mountain waves with meaningful fidelity at 1.5-km resolution [44,52,53]. As a result, these settings could not be used operationally. Output from the current operational configuration of UKV, on the other hand, routinely contains lee wave velocity patterns, when conducive conditions arise.

2.2. The 3DVOM Model

The 3DVOM model uses a finite-difference approach to simulate gravity wave motion, based on a simplified dynamical equation set, to facilitate timely and computationally-efficient provision of lee wave forecasts (Boussinesq, linearised about the background state for a dry atmosphere). The model is described in detail elsewhere, along with some of the case studies that have been used for its validation, as well as the model's strengths and limitations [42,44]. In most cases, the model provides good guidance regarding lee wave activity, particularly in the moderate terrain of the U.K. where the constraint of linear dynamics has limited impact. Furthermore, the incorporation of a parametrisation for boundary layer friction (see below) allows the impact of lee waves on the near-surface wind to be modelled. For instance, it is found that the model simulates particularly strong 10-m wind perturbations clustered in an area to the east of the Pennine hills in northern England, where aviation and high-sided ground vehicles are known to be particularly at risk from the effects of strong winds and turbulence, and another similarly-affected area near the Moray Firth in northeast Scotland [44]. Nevertheless, the linear assumption, absence of moisture processes and uniform background flow assumption can introduce inaccuracies at times. This includes, for instance, flows containing a strong

inversion or particularly strong lee waves, very moist cases weakening the effective stability or causing a lifting instability and cases involving significant convergence or synoptic flow curvature.

To simulate the boundary layer, turbulent mixing is parametrized with a first-order local closure scheme whereby the eddy viscosity $K = l^2 S$, where S is the vertical wind shear and l is a mixing length, defined to be a function of height and stability. The eddy viscosity is partitioned into a background and perturbation contribution, and consistent with the linearization of the momentum equations, the products of perturbation quantities in the turbulent stress terms are assumed small and neglected. Only the vertical gradients of the turbulent stresses are retained in the equations since these are generally much larger than horizontal gradients in the boundary layer.

The model runs over five U.K. domains as follows, of between 100 km and 200 km in scale, which are depicted in Figure 1: Grampians (east Scotland), Pennines (northern England), Northern Ireland, Snowdonia (north Wales) and Dartmoor (southwest England). Model runs are performed at six hourly intervals daily with the first at 00 UTC, with output from each forecast run produced every six hours until T + 48 h.

Data are initially output on all model levels and interpolated to 200-m intervals between 1000 m and 10,000 m ASL for the production of lee wave diagnostics. Archived data, however, are interpolated to a smaller selection of pressure levels: 850, 700, 500, 400, 300, 250, 200 and 150 hPa; and any data analysis over extended periods requires the use of these data and levels.

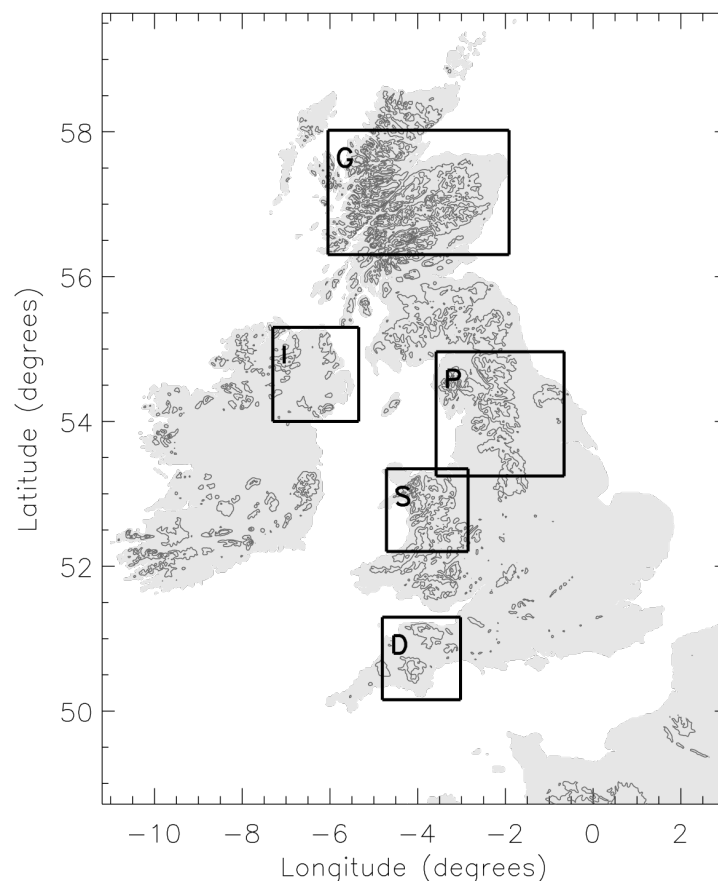


Figure 1. The location of the operational 3D velocities over mountains (3DVOM) forecast domains over the U.K. The labels 'G', 'I', 'P', 'S' and 'D' refer to the Grampians, Northern Ireland, Pennines, Snowdonia and Dartmoor domains, respectively. Also shown are terrain height contours (line contours) at an interval of 200 m.

2.3. BAe-146 Aircraft Observations

2.3.1. Instrumentation

The FAAM aircraft is normally equipped with two independent systems for the measurement of high-frequency, 3D wind components. The core system comprises a 5-port differential pressure system mounted in the nose radome providing measurements of the airflow relative to the aircraft combined with a combined GPS-inertial system for the measurement of the aircraft velocity, attitude angles and their rates of change in Earth-relative coordinates. The operation of this system is described more fully elsewhere [54,55]. Technical limitations due to the need to avoid interference with the operation of the aircraft's standard weather radar mean that the system cannot be de-iced. The second system is an Aventech AIMMS-20 (Airborne Integrated Meteorological Measurement System [56]). This is an instrument package, the external components of which are carried in a standard underwing canister of the kind normally used to carry cloud and aerosol probes. It carries a 5-port differential pressure system in the hemispherical nose of its projecting nose probe. Again, this measures the flow velocity relative to the aircraft (at the instrument location), with a separate combined GPS-inertial system to measure Earth-relative velocity, attitude and attitude-rate information. The instrument carried on the FAAM aircraft differs from that described by Beswick et al. [56] in that its nose probe is de-iced. In order to remove any melt-water that has entered the differential pressure sensor lines, these are connected to a pressure system that can be operated periodically to blow out the lines. This system is fed by a pump carried in the rear of the canister housing, and hence, the GPS-inertial system is mounted internally on an instrument rack within the aircraft cabin. In both systems, the lateral displacement between the differential pressure sensor ports and the GPS-inertial system must be accurately determined in order to calculate terms in the wind velocity equations that are due to the angular rotation of the aircraft [57]. During the flight described, the standard radome with its differential pressure ports was unavailable due to damage from an earlier lightning strike. Hence, we rely solely on the AIMMS-20 probe for the provision of 3D wind components.

2.3.2. Calibration and Quality Control

The AIMMS probe provides both real-time, low-rate and post-flight, high-rate (20 Hz) data. A calibration file maintains the values of key system parameters, including the GPS/INU lateral offsets. These parameters are determined from a standard set of in-flight manoeuvres, which include side-to-side yawing at different airspeeds and a square box pattern of an approximately 1-min duration along the side and with turns of different bank angles between. The calibration constants are derived by optimal estimation to minimize variations in the measured horizontal wind components, which are assumed to be constant during the manoeuvres. Vertical wind measurements from the AIMMS probe remain subject to systematic biases resulting from systematic errors in the input data. For example, a bias of 0.1° in the angle of attack results in a bias of 0.17 ms^{-1} in the mean vertical wind component during straight and level flight. For this reason, it is normal to assume that the mean vertical wind along a straight/level run is zero. The runs considered here have a typical duration of around 30 min and, hence, a length of 180 km at the typical operating true airspeed of 100 ms^{-1} . This represents between 10- and 15-times the typical wavelength of the resonant lee-waves observed, and it is unlikely that mean atmospheric vertical motion on the run length scale will exceed a few $\text{cm}\cdot\text{s}^{-1}$. Hence, the assumption of zero mean vertical wind component over the run length is a reasonable one for the purposes of estimating the lee wave amplitudes.

2.3.3. Flight Day

Flight B890 took place on 6 March 2015. After take-off, the aircraft climbed to 25,000 ft ASL (7.62 km) and flew a total of 8 horizontal legs oriented at true headings of approximately 70° and 250° , approximately parallel to the mean wind direction at altitudes down to 5500 ft ASL (1.67 km), across the Grampian mountains, with an axis over their northern edge.

3. Results

3.1. Lee Wave Statistics

For quick assessment by forecasters, in the past, domain-maximum $|w|$ was used as a summary, using a 'traffic light' system of severity thresholds. Unfortunately, issues such as sensitivity to very localised extremes affect the representativity of domain maxima, leading to high false alarm rates for exceeding standard aviation vertical motion thresholds, particularly for the lowland locations in which airfields are typically located. Meanwhile, a domain mean $|w|$, for instance, will lead to inconsistencies from one domain to the next, depending on the areal fraction containing significant terrain. Therefore, the maximum of the 98th percentile of $|w|$ in each of the diagnostic levels in the domain has been adopted as a simple alternative. This was found, during a careful appraisal of a variety of cases in different domains, to better represent typical by-eye evaluations of wave activity in model fields and can be considered similar to the 'significant wave height' concept in ocean state reporting.

The percentile measure takes a value roughly 50%–60% of the domain maximum $|w|$ in a given domain when discernible wave activity is present. The explanation for this seems to be the occurrence of isolated strong wave crests or troughs, often associated with a single peak in the model terrain. Considering that a square of side equal to a single wavelength occupies of order 1% of the domain area, only a fraction of which corresponds to the largest w values in the wave, the 98th percentile appears to be enough to exclude outlying values of w . At the same time, using the highest percentile that may reliably do this helps ensure that prevalent large amplitude waves are captured.

3.2. Diagnosis of Rotor-Like Patterns in Modelled Near-Surface Winds

A different approach was used to diagnose rotor-like activity in the model. As mentioned in Section 1, the formation of rotors implies wave-induced flow reversal at the surface, which depends on both the wave amplitude and the general strength of the near surface flow [13,14]; a diagnosis of wave amplitude alone is thus insufficient to predict flow reversal. In fact, since both the near-surface flow and the wave amplitude broadly scale with the background wind strength, even very large amplitude waves need not necessarily result in flow reversal. 3DVOM's near-surface flow fields model the impact of simulated waves on the low level winds and can be exploited as a predictor for rotor-like flow reversal.

In highly complex terrain, rotors are unlikely to take the classic quasi-two-dimensional form used in simple conceptual explanations; the near-surface flow is instead imprinted with both the complex structure of wave-induced perturbations and similarly complex direct influence by the terrain. The latter effect could be mitigated by focussing diagnosis on lowland areas downwind of high terrain, where only the remote influence from downwind trailing trapped waves will be felt. However, the 3DVOM domains are of order 100 km wide, and the non-uniform distribution of terrain within each domain means that this is impractical for some synoptic wind directions and is also likely to introduce large biases between different synoptic wind directions. Since direct terrain influence is likely to represent a fairly consistent 'base line' fractional perturbation to the near-surface winds when waves are absent, another option is to determine and subtract this from the total perturbation to quantify the impact of wave activity.

For an automated product, a summary statistic for each domain was required, conveying a broad picture of activity over the domain. Figure 2a,d, respectively, show 3DVOM simulated vertical velocities at 850 hPa and 10-m winds in the Grampians domain for a case where lee waves were weak, so that the pattern of 10-m wind was dominated by local terrain effects. Subsequent columns in Figure 2 demonstrate the increasing influence of lee waves on the near surface flow, as the 10-m winds become increasingly decoupled from local terrain features and instead coupled to the pattern of wave motion aloft.

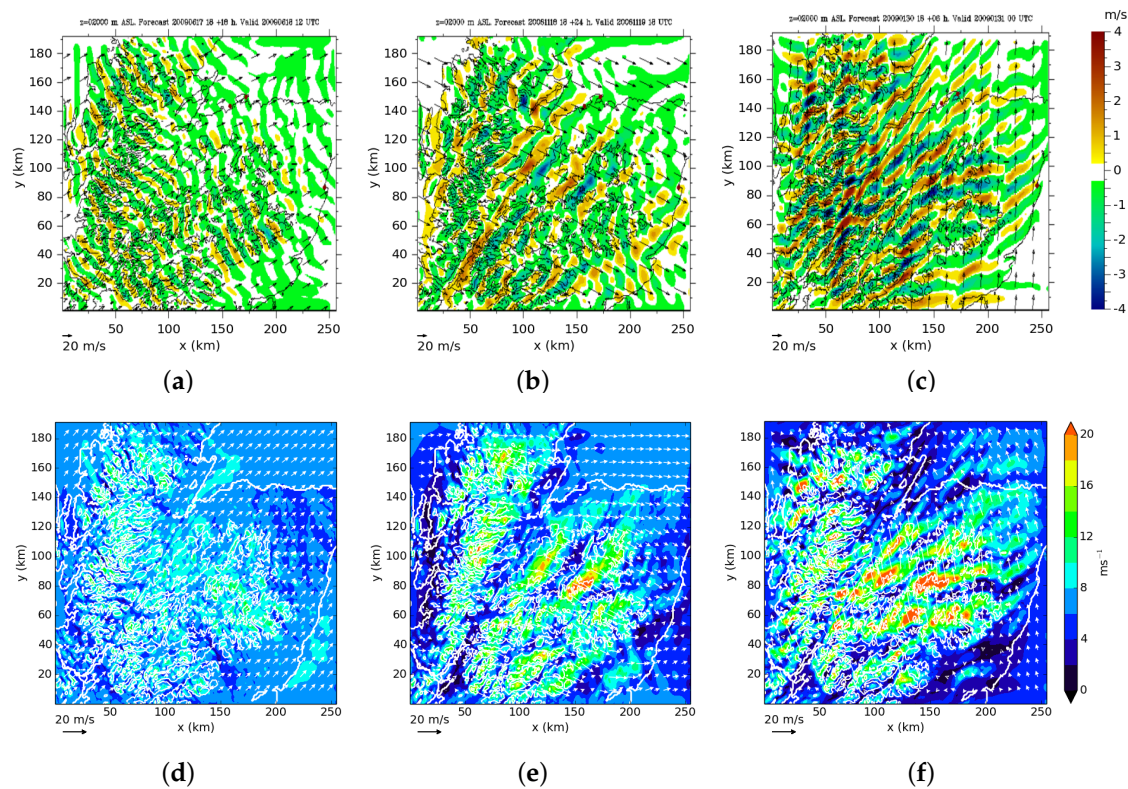


Figure 2. (a–c) w at 2000 m ASL and (d–f) 10-m winds for the Grampians 3DVOM domain at: (a,d) 12 UTC 18 June 2009 ($|\overline{\mathbf{u}}_{10m}| = 7.05 \text{ ms}^{-1}$, $|\overline{w_{850hPa}}| = 0.268 \text{ ms}^{-1}$, $|\overline{\Delta s}| = 0.163$); (b,e) 18 UTC 19 November 2008 ($|\overline{\mathbf{u}}_{10m}| = 7.02 \text{ ms}^{-1}$, $|\overline{w_{850hPa}}| = 0.45 \text{ ms}^{-1}$, $|\overline{\Delta s}| = 0.383$); (c,f) 00 UTC 31 January 2009 ($|\overline{\mathbf{u}}_{10m}| = 7.00 \text{ ms}^{-1}$, $|\overline{w_{850hPa}}| = 0.781 \text{ ms}^{-1}$, $|\overline{\Delta s}| = 0.611$).

The caption in Figure 2 lists values for the following statistics from each simulation for the snapshot shown: the domain mean 10-m wind vector magnitude, $|\overline{\mathbf{u}}_{10m}|$, the r.m.s. $|w|$ at the 850-hPa level, $|\overline{w_{850hPa}}|$, and the value of $|\overline{\Delta s}| = \overline{(|u_{10m} - |\overline{\mathbf{u}}_{10m}||) / |\overline{\mathbf{u}}_{10m}|}$. Here, \mathbf{u}_{10m} represents the 10-m wind at a point resolved in the direction of the domain mean, and $|\overline{\Delta s}|$ represents the domain mean fractional perturbation of the wind. When the local $|\Delta s|$ exceeds one, this either reflects flow reversal (notionally associated with flow separation and, hence, rotor formation) or an equivalent speed-up of the wind. Often, in idealised rotors, both of these occur together, with waves causing roughly equivalent wind perturbations in either sense. Note that while large local values of the perturbation quantities exist within each snapshot, the domain mean values are considerably smaller, since their variation is wavelike.

The wave field at the 700-hPa level (roughly 3000 m ASL) is quite similar to that at 850 hPa, and being further from the terrain, w at this level might be expected to give a “purer” measure of lee wave activity compared to w at 850 hPa, especially in the Grampians domain. However, the latter level has been taken to give the relevant measure of wave amplitude, since $\overline{|w|}$ at the lowest of all available (archived) levels was found to correlate most closely with $|\overline{\Delta s}|$ in strong wave events. The correlation is evident from the numbers quoted in the caption. Almost identical $|\overline{\mathbf{u}}_{10m}|$ has been diagnosed for all three examples; this is important since wave amplitude scales with the speed of wind encountering terrain, with the limiting case near the surface that w is proportional to the terrain slope \times the wind speed. Δs tends to diverge at low wind speeds as unorganised perturbations become comparable in strength to the mean wind (in real flows, this is exacerbated by a spectrum of turbulent motions stretching to small scales), so cases with fairly large $|\overline{\mathbf{u}}_{10m}|$ have been used for the comparison. Thus, in Figure 2, the variation of wave amplitude between cases reflects the conditions for resonant wave

trapping, rather than variation in background wind speed. Likewise, increasing perturbations of the 10-m wind from case to case reflect the increasing influence of the wave field aloft.

This is visualised more generally in Figure 3a,b, scatter plots of $|\overline{w_{850hPa}}|$ vs. $|\overline{u_{10m}}|$ for the Pennines and Grampians domains (in which mountainous terrain and strong lee waves are common; the behaviour for other domains is qualitatively similar). Points are also coloured to depict the variation of $|\overline{\Delta s}|$. Data are plotted only for values of $|\overline{u_{10m}}| > 5 \text{ ms}^{-1}$, due to the above-mentioned breakdown of correlation between quantities at low wind speeds and to exclude lee waves not posing a significant hazard. Correlation between the three quantities is clear: stronger winds lead to larger amplitude waves, and for a given wind speed, stronger waves are linked to more dramatic near-surface wind disturbance. A lower bound on $|\overline{w_{850hPa}}|$ may also be inferred for a given $|\overline{u_{10m}}|$, which we posit is related to the direct influence of the terrain. Values of $|\overline{\Delta s}|$ are similar at this lower bound regardless of wind speed, since $|\overline{\Delta s}|$ is a dimensionless quantity, by definition scaled for background wind. For a given wind speed, as wave activity increases, $|\overline{\Delta s}|$ also increases, scaling according to $|\overline{w_{850hPa}}|$ minus the lower bound. Thus, isolines of $|\overline{\Delta s}|$ lie parallel to the lower bound, increasing as $|\overline{u_{10m}}|$ increases. This results in the ordered, slanted ‘rainbow-like’ arrangement of colours seen in Figure 3a,b. This behaviour is mirrored in all of the 3DVOM domains, with a similar spread of $|\overline{w_{850hPa}}|$ vs. $|\overline{u_{10m}}|$ for each. Meanwhile, terrain differences in each domain mean that the slope and intercept of the plot, and values of $|\overline{\Delta s}|$, differ significantly, with higher values of $|\overline{w_{850hPa}}|$ and $|\overline{\Delta s}|$ occurring for a given $|\overline{u_{10m}}|$ in more mountainous domains.

It seems reasonable to suggest that the silhouette area of the terrain in the domains used is sufficiently isotropic that the interdependence in Figure 3a,b does not vary strongly with wind direction (we will return to this below); in which case, Figure 3a,b represent a complete summary of wind perturbation by lee waves that can be simply rescaled for different domains. This offers a pathway to a single diagnostic approach for rotor-like activity across domains. Considering first a single domain, $|\overline{\Delta s}|$ can be diagnosed directly and a threshold applied consistent with likely flow separation. However, $|\overline{\Delta s}|$ also increases with $|\overline{w_{850hPa}}|$. Thus, $|\overline{w_{850hPa}}|$ can likewise be used to infer the likelihood of rotor activity. Given the sensitivity of near-surface flow reversals to numerous model factors, the scatter inherent in $|\overline{w_{850hPa}}|$ and $|\overline{\Delta s}|$, the relative reliability of gravity wave amplitude (i.e., $|\overline{w_{850hPa}}|$) forecasts compared to surface wind perturbation forecasts (i.e., $|\overline{\Delta s}|$) and the heuristic idea that large amplitude waves at low levels enhance surface effects, an approach incorporating both $|\overline{\Delta s}|$ and $|\overline{w_{850hPa}}|$ has been adopted. The diagnostic is expressed by the following rules, which when satisfied trigger a warning of a ‘risk of rotor activity’,

- (i) $|\overline{u_{10m}}| > 5 \text{ ms}^{-1}$ and lee waves of moderate or greater amplitude diagnosed
- (ii) $|\overline{w_{850hPa}}| > w_{crit}$ and $|\overline{\Delta s}| > \Delta s_{crit}$
- or
- (iii) $|\overline{w_{850hPa}}| > w_{crit} + 0.1 \text{ ms}^{-1}$

where w_{crit} lies 0.2 ms^{-1} above the lower bound described above with reference to Figure 3a,b and is diagnosed from equivalent plots for each domain. The value of 0.2 ms^{-1} has been chosen empirically. Δs_{crit} was determined from the values of $|\overline{\Delta s}|$, which occur in the data (e.g., Figure 3a,b) close to w_{crit} . For speed and simplicity, this was done by eye; a more rigorous approach would likely yield similar values. Values of 0.19 and 0.25 for the Pennines and Grampians domains were determined, respectively, for instance. Rule (iii) relaxes the condition regarding $|\overline{\Delta s}|$ if the wave amplitude is particularly large. This ‘belt and braces’ combination should reduce false alarms, while minimising arbitrary misses through flexibility in how severe cases are captured. While the statistical nature of the method means that a warning might be triggered when in fact $|\overline{\Delta s}|$ is nowhere one or greater within the domain, this can still be taken to imply that rotor activity is more likely (taking into account uncertainty in the model wind field forecast). The term ‘risk of rotor activity’ does not express a specific quantity of risk, but is considered a simple, useful indicator for forecasters of an extant potential hazard.

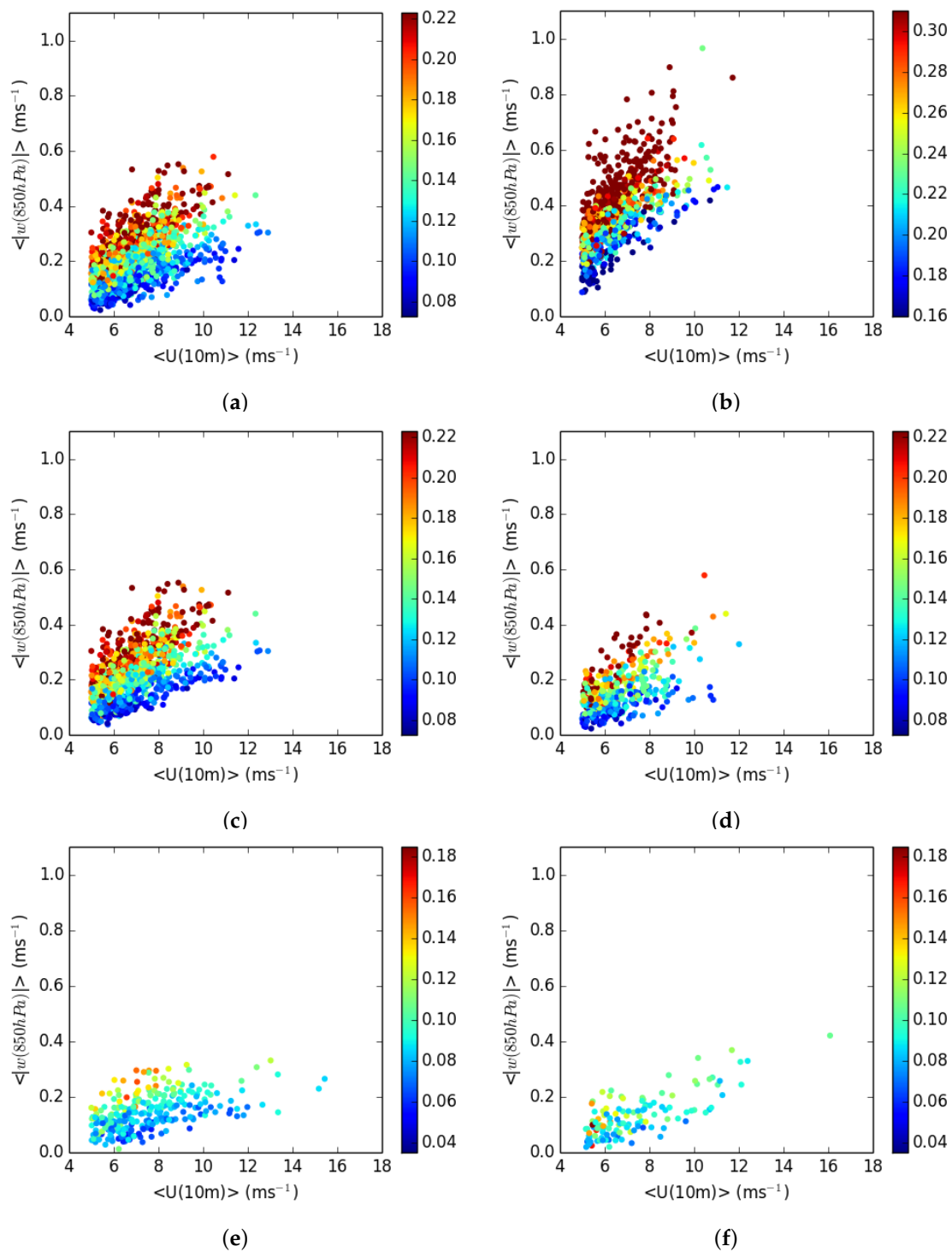


Figure 3. Variation of $|\overline{w_{850hPa}}|$ as a function of $|\overline{\mathbf{u}_{10m}}|$ for 3DVOM forecasts from 2007–2010 for (a) the Pennines domain and (b) the Grampians domain. Values of $|\Delta s|$ are highlighted using colour. (c,d) are as (a), but filtered for $\overline{\mathbf{u}_{10m}}$ containing (c) a westerly and (d) an easterly component. (e,f) are as (c,d), but for the Dartmoor domain.

The assumption that wind direction plays no strong role in the variation in Figure 3a,b is examined in Figure 3c,d, which splits the data for the Pennines domain into cases with a westerly or an easterly component in $\overline{\mathbf{u}_{10m}}$. The behaviour is qualitatively the same, and the quantitative differences seem

small enough to neglect for simplicity. The perhaps slightly smaller $|\overline{w_{850hPa}}|$ values associated with a given $|\overline{u_{10m}}|$ and $|\Delta s|$ in Figure 3d are presumably related to the frequent presence of a low-level subsidence inversion in anticyclonic easterly flows. Δs tends to be larger for a given wave amplitude for these flows [14], while the strong stability associated with the inversion results in relatively short wavelengths, which may not be fully resolved, leading to underestimation of their amplitude (the concept of ‘effective resolution’ suggests only wavelengths above 8 km will be fully resolved). Similar behaviour occurs for the other domains; equivalent plots for the Dartmoor domain are shown in Figure 3e,f.

The validity of the diagnosis approach was monitored by subjective inspection of numerous example cases up to and following operational implementation. Figures 4 and 5 depict maps of w_{850hPa} and 10-m wind for several such cases with an emphasis on ‘edge’ cases close to the thresholds used for diagnosis. For each of these cases and those in Figure 2, Table 1 lists dates, values of $|\overline{u_{10m}}|$, $\hat{w}_{850hPa} = |\overline{w_{850hPa}}| - (w_{crit} - 0.2 \text{ ms}^{-1})$, $|\Delta s|$ and corresponding classification in terms of wave severity and whether or not a ‘risk of rotor activity’ is posed. \hat{w}_{850hPa} expresses the ‘net’ vertical motion due to waves.

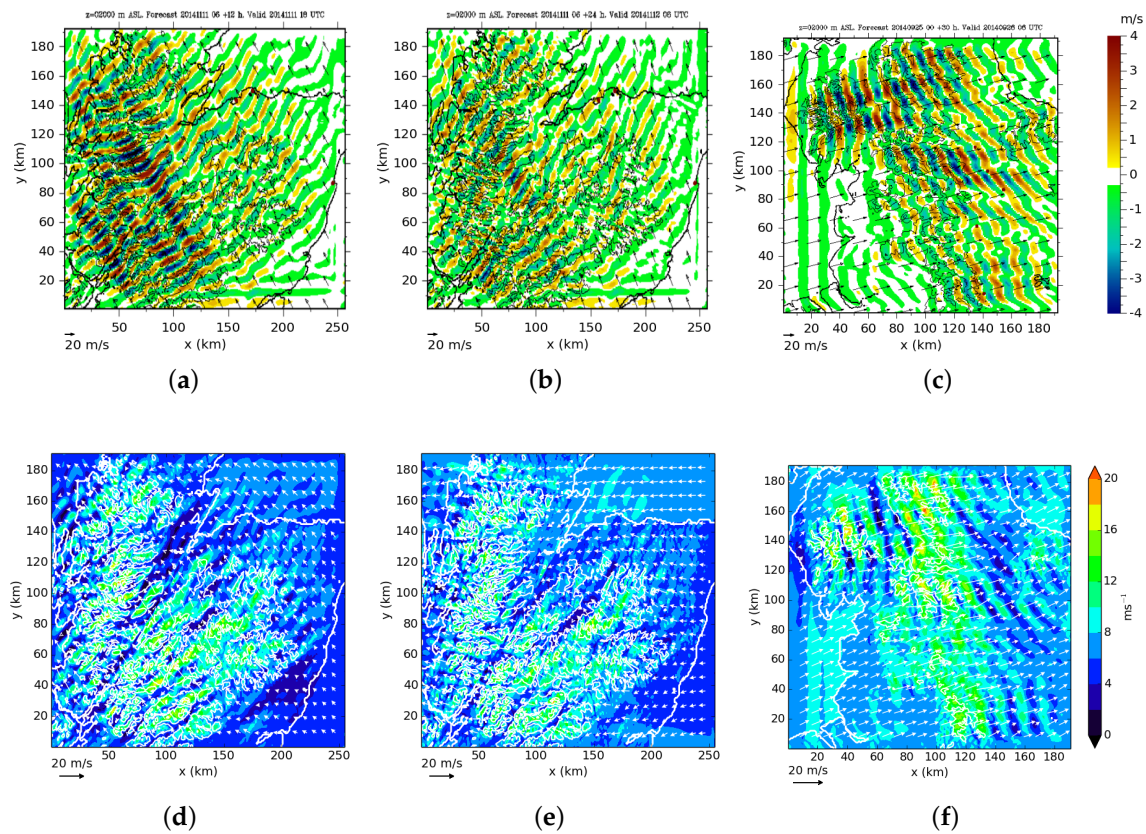


Figure 4. As Figure 2, but for the Grampians domain at (Left) 18Z 11 November 2014, (Center) 06Z 12 November 2014 and (Right) the Pennines domain at 06Z 25 September 2014.

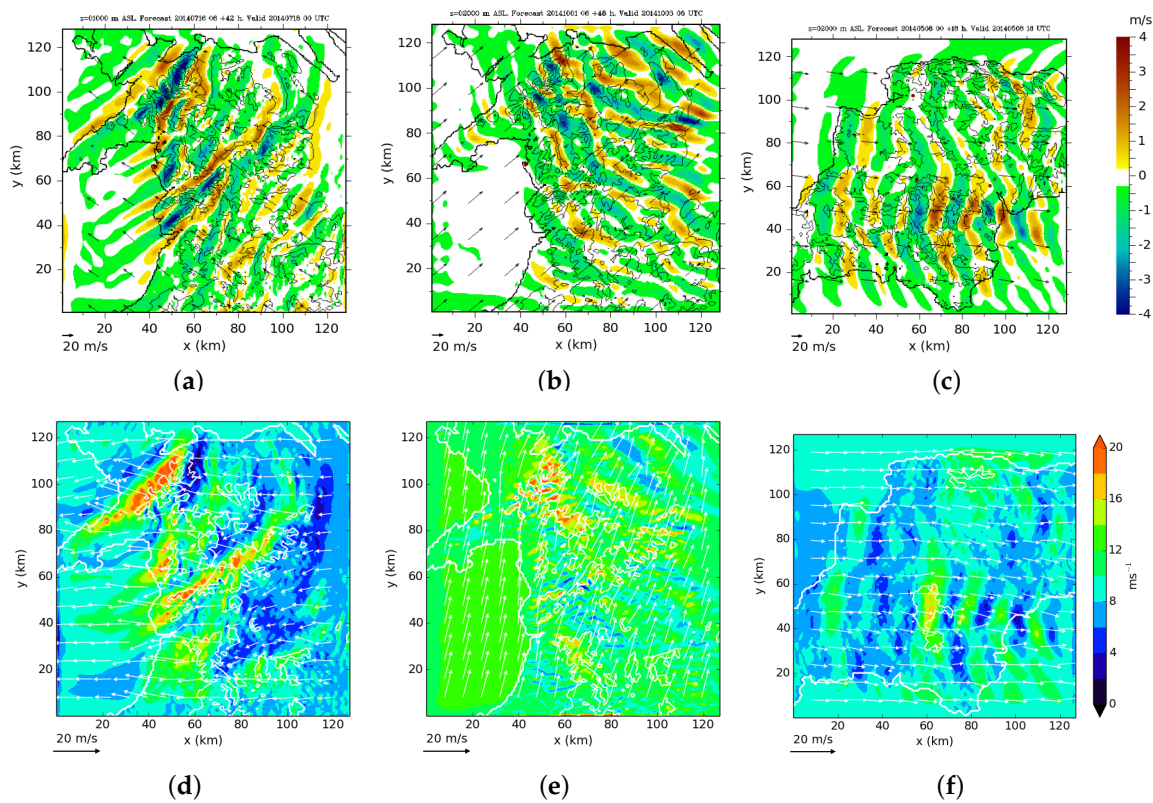


Figure 5. As Figure 2, but for the Snowdon (north Wales) domain at (Left) 00Z 18 July 2014 (w at 1000 m shown), (Center) 06Z 3 October 2014 and (Right) the Dartmoor domain (southwest England) at 18Z 8 May 2014.

Table 1. Characteristics of case examples plotted in Figures 2, 4 and 5 (see the text for the explanation). The diagnosed wave severity is given in the penultimate column. Indication of whether rotor risk warnings are triggered by \hat{w}_{850hPa} exceeding 0.3 ($'w'$), $|\Delta s|$ exceeding $|\Delta s|_{crit}$ ($'\Delta s'$) or both is indicated in parentheses in the final column.

Case (Figure)	Validity Time (UTC, dd/mm/yy)	Domain	$ \overline{u}_{10m} $ (ms^{-1})	\hat{w}_{850hPa} (ms^{-1})	$ \Delta s $ ($ \Delta s _{crit}$)	Wave sev.	Rotor Risk (Trigger)
1 (4)	18, 11/11/14	Grampians	6.13	0.553	0.327 (0.250)	severe	yes ($w + \Delta s$)
2 (4)	06, 12/11/14	Grampians	6.35	0.288	0.249 (0.250)	moderate	no
3 (4)	06, 25/09/14	Pennines	8.03	0.429	0.211 (0.190)	moderate	yes ($w + \Delta s$)
4 (5)	00, 18/07/14	Snowdon	8.67	0.245	0.227 (0.180)	moderate	yes (Δs)
5 (5)	06, 03/10/14	Snowdon	11.20	0.246	0.145 (0.180)	moderate	no
6 (5)	18, 08/05/14	Dartmoor	8.44	0.301	0.145 (0.150)	moderate	yes (w)
(2)	12, 18/06/09	Grampians	7.05	0.056	0.163 (0.250)	nil	no
(2)	18, 19/11/08	Grampians	7.02	0.262	0.383 (0.250)	moderate	yes (Δs)
(2)	00, 31/01/09	Grampians	7.00	0.624	0.611 (0.250)	severe	yes ($w + \Delta s$)

The different cases where a ‘risk of rotor activity’ is highlighted show good consistency between domains in the appearance of wave-induced disturbances in the 10-m wind field. The ‘edge’ cases illustrate the boundary where the wave impact is considered marginally too bland, or marginally enough, to report as a ‘rotor risk’. In Case 2, a risk is very nearly triggered by the value of $|\Delta s|$, while Case 1 is a clear-cut report on the basis of large values of both \hat{w}_{850hPa} and $|\Delta s|$. Case 3 is similar. Case 6 is just barely reported as a ‘rotor risk’, on the basis of \hat{w}_{850hPa} alone (though $|\Delta s|$ is also close to the trigger threshold). Overall, it is clear that strong wave cases (in some instances, not shown, severe waves) are not necessarily synonymous with the issuance of a ‘rotor risk’ warning, nor more moderate

waves with its absence, consistent with our earlier statement and the mechanism described in the literature [11,13,14].

The wave and rotor activity diagnostics described are per domain; more fine-scale guidance would require a smaller scale analysis. Thus, guidance specific to lowland areas some distance downwind of terrain is not within the scope of the diagnostic as it stands. Nevertheless, widespread lee waves with a long decay scale, affecting such areas, will lead to larger values of $|w_{850hPa}|$ and $|\Delta s|$ than waves that decay quickly downwind and a correspondingly more severe diagnosis that can be used to infer the likelihood of downwind impacts.

3.3. Simulation of Lee Waves within UKV

In this section, UKV forecasting of a case study of lee waves over Scotland is discussed and compared with aircraft- and surface-based measurements to demonstrate the efficacy of UKV in simulating lee waves, using the current lee wave forecasting system (3DVOM) as a benchmark.

3.3.1. Case Study: 6 March 2015

Comparisons with a flight carried out on 6 March 2015 over the Grampian mountains, Scotland, are presented. A UKV forecast initiated at 09 UTC was used since the flights occurred shortly after this time. Vertical cross-sections through the simulated wave field (not shown) indicate near vertical wave phase lines, suggesting waves strongly trapped within the troposphere, with a horizontal wavelength around 15 km in the lowest 2–3 km. Comparison of the UKV model forecast vertical velocity field with the aircraft measurements in Figure 6 shows that the simulated waves correspond fairly closely to the observations. The phase and amplitude of the waves are reproduced faithfully by the model at upper levels. At the lower four levels, phase and wavelength are broadly reproduced, though amplitude is a little weak in the western half of the plot. In 3DVOM, meanwhile (again, Figure 6), the wavelength is generally somewhat too short, while amplitudes are much larger, at times significantly greater than those observed. The reason for this overprediction has not been examined in detail, though the effects of moisture in UKV have been investigated for another case by performing an equivalent simulation without moisture. This resulted in an increase in amplitude comparable to the overprediction of 3DVOM here and a decrease in wavelength. As mentioned earlier, the concept of “effective resolution” suggests only wavelengths above 8 km will be fully resolved in 3DVOM and those above 12 km in UKV. However, wavelengths in this case (discernible from Figure 8) are somewhat greater than 12 km.

A broad qualitative validation of the UKV wave field can be made by comparing satellite cloud images with top-of-atmosphere (TOA) shortwave radiation from UKV (which reveals the cloud structure visible from above). Figure 7 shows this comparison at 10 UTC on 6 March (high cloud obscured wave patterns in later satellite images, whereas at 10 UTC, only the northwestern corner of the view was obscured). A similar wave pattern exists in both the satellite image and the model cloud, with comparable wavelengths in a given area and roughly v-shaped wavefronts over the central highlands, becoming more linear over lower land closer to coastal areas and in the east, while generally clearing (suggesting net descent) eastward (leeward) of the highland areas.

It is also informative to compare lee wave vertical motion and wave-perturbed near-surface winds in UKV and 3DVOM over the Grampians domain. Figure 8a,b and Figure 8c,d compare w at 2-km and 10-m winds, respectively, for 3DVOM and UKV at 12 UTC for this case. The wave patterns in each model are somewhat similar, with the strongest vertical velocities in comparable areas; four SW-NE running stripes of stronger vertical velocities are particularly clear in 3DVOM centred at around $(x = 75 \text{ km}, y = 160 \text{ km})$, $(x = 75 \text{ km}, y = 100 \text{ km})$, $(x = 120 \text{ km}, y = 80 \text{ km})$ and $(x = 210 \text{ km}, y = 60 \text{ km})$ in the figure, partly since vertical velocities are somewhat higher in 3DVOM (reflecting the comparison in Figure 6). These areas correspond to large variation of terrain height in the along-wind direction. The v-shaped wavefronts seem less apparent in 3DVOM, perhaps due to differences in the simulation of interference in the two models. Lee-wave-induced perturbations in the 10-m wind are comparable in magnitude in both models, though in Figure 8c, patterns seem to reflect the more linear

wavefronts occurring in 3DVOM, and 10-m winds are slightly weaker overall in UKV. Variation in synoptic wind conditions is apparent in UKV, with stronger winds in the northwest of the domain (most noticeable over the sea). This is absent in 3DVOM, which is constrained by a horizontally homogeneous background flow.

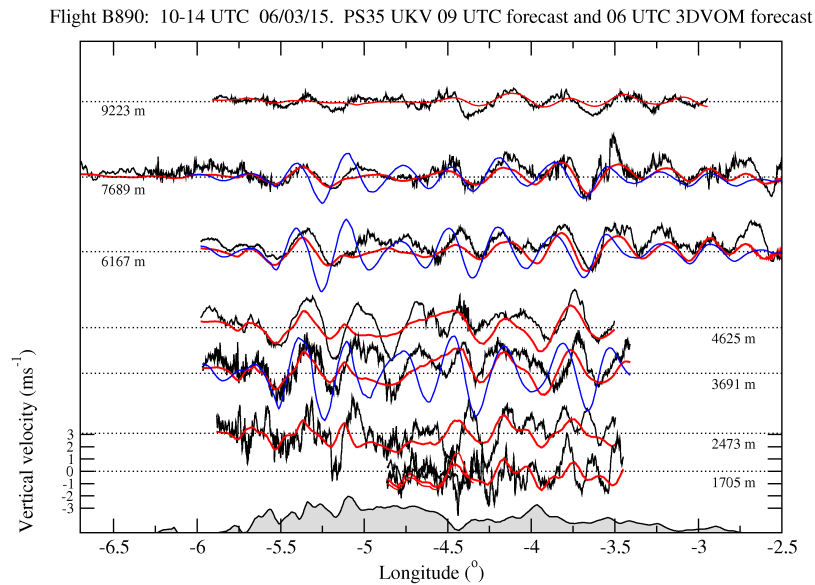


Figure 6. Comparisons of model vertical velocity with Facility for Airborne Atmospheric Measurement (FAAM) observations on 6 March 2015. The observations are shown in black (ms^{-1}) along the horizontal flight legs with the underlying orography. The forecast vertical velocity from the UKV model using the ENDGame core, initiated at 09 UTC, are interpolated onto the aircraft trajectories, shown in red. Hourly forecast data are selected according to the closest hour to the mid-point time of each aircraft leg. Also shown are vertical velocities from the 06 UTC 3DVOM forecast (blue) valid at 12 UTC along three of the aircraft legs.

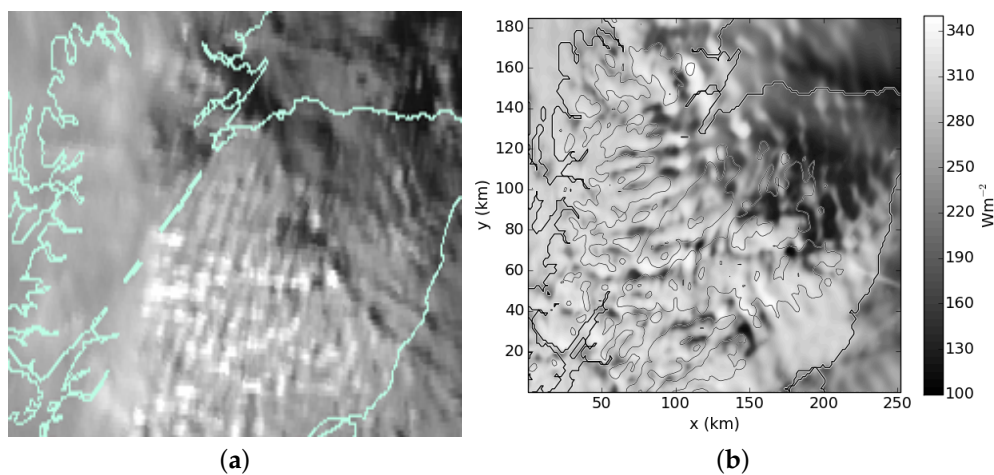


Figure 7. (a) Meteosat Second Generation visible satellite image at 10 UTC 6 March 2015, cropped over the Grampians 3DVOM domain region; and (b) UKV TOA shortwave radiative flux cropped to the same area. Note, no effort has been made to synchronise the shading scales of the two panels, so they may only be compared in a qualitative sense.

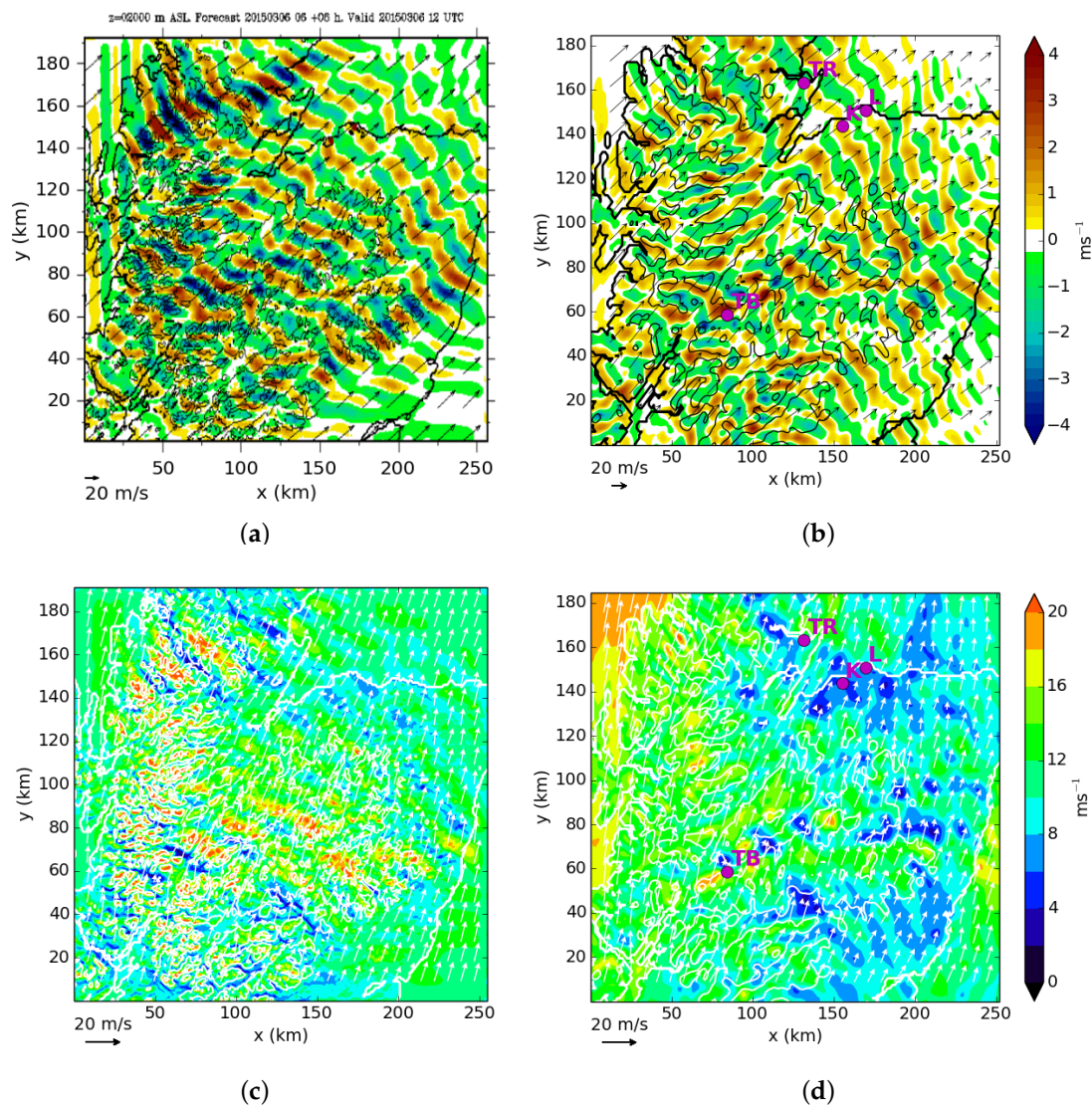


Figure 8. w at 2000 m ASL from (a) the operational 3DVOM run; (b) UKV with ENDGame core; and 10-m wind from (c) 3DVOM and (d) UKV with ENDGame core, valid at 12 UTC 6 March 2015. Locations of surface observing sites ‘Tain Range’ (TR), ‘Tulloch Bridge’ (TB), ‘Kinloss’ (K) and ‘Lossiemouth’ (L) are marked in (b, d).

It is generally difficult to conclusively study lee wave effects at the surface in detail without a dense array of measurement sites, preferably involving microbarographs and a reference location upwind of any hills [14,28]. However, signatures of lee waves should be detectable in the variation of routine surface wind observations over time, for instance as they are affected by the procession of lee wave troughs and crests overhead in a wave field evolving in response to changing upwind conditions. If similar signatures appear in forecast models in the same period, this represents an encouraging indicator that models can offer useful guidance concerning these effects. Winds at 10 m at four synoptic observation sites within the Grampians domain (marked in Figure 8b,d) are plotted in Figure 9 alongside 10-m winds extracted from grid boxes in the UKV and 3DVOM models containing the same locations. Since the UKV winds represent instantaneous values and 3DVOM winds are only supplied six-hourly, one-minute observed wind data are shown in addition to hourly averages. Global model data for the same locations and times are also included; with no resolution of lee wave effects, the global model indicates the trend in the larger scale synoptic wind patterns, unperturbed by lee

waves, and has some correspondence with the boundary forcing applied in the finer scale models. A UKV forecast initiated at 03 UTC was used in order to provide coverage of the wave evolution throughout the day.

In Figure 9a, showing winds at ‘Tain Range’, the global model indicates a steady rise in 10-m wind as a cyclone approaches over Scotland from the west. In both of the fine-scale models, a slow decline commences against this trend in the late morning, and this reflects the spread eastwards of the lee wave crest that can be seen just to the west in Figure 8b,d. A similar decline, though displaced a little later, occurs in the observed winds, suggesting that this is indeed due to lee wave motion overhead, captured reasonably well by UKV. 3DVOM, meanwhile, is less well timed and over-forecasts variability. In UKV, by 17 UTC, an area of winds exceeding 20 ms^{-1} (roughly three-times the wind at Tain Range) grows just offshore to the northeast, just outside the area covered by the figure, accompanying the following wave trough. This reflects the challenge of forecasting wind variations correctly on these scales.

Figure 9b shows winds at ‘Tulloch Bridge’. Again, the global model conveys the steady rise in synoptic winds throughout most of the day. The initial rise is also present in the observations and reflected in UKV. At 06 UTC in UKV, the lee wave crest overhead strengthens, resulting in a dramatic drop in 10-m wind. The stronger part of the crest then migrates west, and the wind recovers. A similar drop occurs in the observed wind at the same time, suggestibly for the same reasons, though a second drop reaching a minimum at 09 UTC is not captured in UKV, the simulated wind in fact increasing, until it exceeds that at 10 m in the global model for a time (as eventually do the observed winds). During the subsequent change in structure and intensity of the wave field, the 10-m wind at Tulloch Bridge in UKV drops again, from 12 UTC. A similar drop, though occurring a little later (from 15 UTC), is also evident in the observed wind. As already established, 3DVOM appears to over-forecast the strength of the wave activity on this date. 3DVOM places this location beneath a lee wave crest throughout the day, suppressing the winds at all times well below the global model prediction for the area, poorly representing observations.

Figure 9c,d depict winds at Kinloss and Lossiemouth, respectively, two stations about 18 km apart in the along-wind (in this case) direction. The global model winds indicate again a broad increase of synoptic winds over the period shown. Over Kinloss, initial evolution of the wave field in UKV is rapid, with contraction and then expansion of the lee wave wavelength leading to a crest passing overhead first upwind and then downwind, creating wind minima at 09 and 11 UTC. Evolution is subsequently slower, with a further wave crest gradually passing overhead between 14 and 22 UTC, with an accompanying drop in winds. Following this, the wave field dissipates, and winds accelerate. At Lossiemouth (Figure 9d), the first of these crests passes over at 16 UTC, again with a drop in winds, and the second does not arrive before dissipation of the waves. A further downwind crest, which never approaches Kinloss, also passes over Lossiemouth earlier at 09 UTC, reducing 10-m wind speed. Observations at Kinloss indicate undulations of the wind centred around 10 UTC, which may correspond to the early evolution of the wave field, though with somewhat different timing to the UKV time series, while a period of reduced winds between 1230 and 1930 UTC may correspond to a second, slower moving crest as seen in UKV. Meanwhile at Lossiemouth, a stall in ramping up of the winds around 07 UTC and a minimum at 17 UTC may be responses to wave crests akin to those simulated by UKV. A further minimum in winds at both sites at about 2130 UTC was observed, but not simulated by UKV, and may relate to inaccuracies in representing the dissipation phase of the waves. 3DVOM forecast data at Lossiemouth are available only when the location was not affected by troughs or crests, and the model places Lossiemouth in a neutral position with respect to both at each time, while substantial wave-induced accelerations and decelerations are simulated nearby. Kinloss is placed beneath a lee wave trough at 18 UTC and at the edge of a crest at 00 UTC. Again, the over-forecast of wave amplitude leads to a large error at 18 UTC.

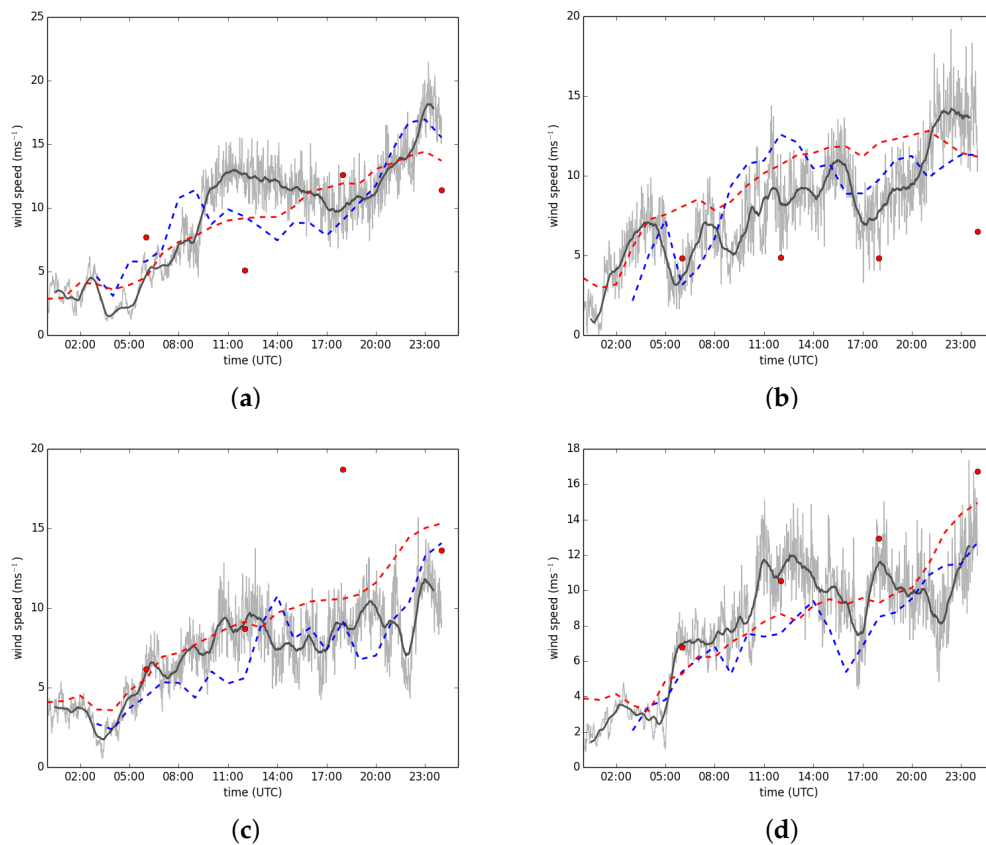


Figure 9. Time series of 10-m winds observed on 6 March 2015 at four Met Office synoptic stations at 1-min intervals (light grey) and as a moving average over 1 h (dark grey) and forecast hourly (instantaneous values) by UKV (blue dashed) and the Met Office global model (red dashed) and six-hourly by 3DVOM (red filled circles) in the grid box containing the same site: (a) Tain Range; (b) Tulloch Bridge; (c) Kinloss; and (d) Lossiemouth; locations marked in Figure 8b,d.

As described in Section 2.2, 3DVOM assumes a steady background state. This may have an effect on the relative level of agreement seen for 3DVOM and UKV, since time variation of the background induces transient effects that are not explained by the instantaneous background conditions at a given time. It was found, however, that the UKV wave fields are slowly varying in this case. For example, the comparisons of UKV vertical velocity fields with aircraft data in Figure 6 are not greatly sensitive to the forecast hour chosen (using model data from an hour earlier or later makes little difference). It has been demonstrated that an evolving wave field (in a time-varying mean flow) can be regarded as a sequence of steady states if the background flow remains steady over the time taken for wave packets to propagate over several horizontal wavelengths [43]. For typical tropospheric mountain waves, this time scale is generally less than 1 h.

Winds at five other sites within the domain were available. In all cases, the most dramatic lee wave effects at the surface in the models occur by chance away from any observation locations (such as the deceleration region just to the west of Tain Range in Figure 9d), suggesting that lee wave surface effects are not particularly observationally well sampled, and making 10-m wind variations observed more modest and difficult to attribute. In general though, across all sites, variability was observed with broadly the same time scales and amplitudes as the lee wave effects forecast by UKV at the same locations. While we cannot discount the possibility of large lee side eddies or complex non-linear effects or scale interactions not represented in the models as the cause of the wind effects observed, the above comparisons suggest reasonable forecastability of lee wave surface impacts by UKV. This

supports confidence in the usefulness and representativity of the automated diagnostic for 'risk of rotor activity', once adapted for use with UKV.

4. Discussion

The lee wave and 'risk of rotor activity' diagnosis method developed for 3DVOM aims at simplicity and robustness. It involves a straightforward statistical calculation and rule set, which can be easily adapted to new domains. It takes advantage of inherent mutual correlations between wind speed, wave amplitude (reflecting the atmospheric stability) and near-surface wind perturbation, determined by the terrain characteristics, which do not vary fundamentally from one domain to the next. The statistical, areal approach removes any need to map out fine-scale terrain influence or use a function of wind direction, while the output summary statistics are amenable to potential use within a probabilistic framework. By utilising a net lee wave contribution to vertical motion, the approach becomes easily adaptable to different model resolutions (where direct terrain effects be different), so long as lee waves are well resolved.

Nevertheless, there is scope for further refinement, for instance through more systematic study of how near-surface wave-induced wind perturbations are related to the three-dimensional wave structure aloft (such as the vertical distribution of wave activity). The effect of lee wave wavelength has also not been accounted for. The measure of "direct terrain influence" derived effectively represents flow perturbation in neutral conditions. An alternative approach might involve adaptation of known results for neutral flow over idealised terrain or a simple-minded 2D estimate of flow perturbation, based on the mean flow near the surface and terrain gradients within the domain. Though consciously avoided here, an ancillary map of fine-scale direct terrain influence as a function of background wind speed and direction might afford more fine-grained diagnosis of wave effects, if a robust and straightforward method could be found.

Routine operational NWP model forecasts are clearly at the point of being able to produce credible simulations of lee wave activity, which verify well against direct observations and existing lee wave forecasting methods. Supplanting the latter using routine NWP output would help simplify and unify the source of forecast data. For the case of the 3DVOM model, the advantages of using UKV with the ENDGame dynamical core to do this are listed below and are illustrative of advantages compared to simplified standalone/offline techniques in general:

- No simplifying (linear) approximations applied to the model equations of motion; the most hazardous mountain wave flows are highly non-linear, e.g., rotors and hydraulic jumps/wave breaking
- Realistic initial and boundary conditions, data assimilation, representation of convergence and convection; problems can occur in 3DVOM when there is significant horizontal variation in conditions and atmospheric forcing (e.g., trough or low centre within the domain), since it is initialised by a single profile
- Thorough representation of moist processes (noting that the U.K. has a very moist climate with cloud and rainfall common); 3DVOM is a dry model, but in reality, reversible latent heating (cloud formation and evaporation) effects favour flow over terrain rather than blocking, also affecting wave amplitude [58]; meanwhile, irreversible latent heating effects (e.g., upslope rainfall) modify the stability profile and, hence, the wave response [59–62]; further, any orographically-triggered deep convection will negate wave activity
- More sophisticated boundary layer scheme; the boundary layer is known to impact lee wave generation and downwind decay [63–65], while the performance of the boundary layer scheme also decides the accuracy of forecast lee wave impacts on near-surface winds [13,44]
- Direct simulation of the diurnal cycle through radiation, surface and boundary layer parametrisations, including for instance nocturnal stable boundary layers; boundary layer stability strongly affects wave propagation and lee wave decay [64]

- Full and contiguous coverage of the U.K. (and eventually beyond, as future computing resources allow)
- Lee wave impacts become prognostic; the interplay of lee waves with the atmospheric environment in which they form, including other weather phenomena, is represented
- Access to a comprehensive, standardised set of diagnostics, long-term central archiving

Regardless of the precise impact of these improvements, the knowledge that relevant processes and effects in lee wave cases are represented with greater rigour adds confidence to UKV forecasts of lee wave activity; the level of agreement between 3DVOM and UKV and the ability to attribute disagreements is reassuring, affording a degree of mutual affirmation between existing and future methods. On the other hand, the simplicity of 3DVOM offers a degree of transparency and ease of interpretation; in UKV, many different effects in addition to lee wave signatures may combine simultaneously, perhaps in different areas of the domain, so that caution must be used in the adaptation of lee wave and ‘risk of rotor activity’ diagnostics. The extensive UKV domain (compared to 3DVOM) means that, to map out wave activity, an approach summarising impacts over a local area, rather than a domain, would be needed. This would require the creation of a selection of ancillary datasets to replace information currently specified ‘per domain’ with equivalent ancillary information on the UKV grid. In addition to wave activity, convection is another source of strong vertical motion and disturbed surface winds, so that lee wave diagnosis would have to distinguish between resolved convection and wave activity, perhaps using vertical profile information, patterning characteristics (signatures of either wavelike or convection-like horizontal variation, orientation of structures with respect to wind direction), precipitation intensity and variation, etc. Once diagnostics are finalised, their instatement as standard UKV diagnostics would allow their easy integration into downstream products, such as hazard models.

The concepts of wind speed-dependent perturbation used in this study with regards to $|\overline{\Delta s}|$ and \hat{w}_{850hPa} are similar to ideas used in gust forecasting, where methods tend to predict gust magnitudes roughly proportional to grid box wind speed. In very high resolution models, large, unrealistic gusts may be output by standard gust prediction algorithms over rugged terrain. This is because these algorithms (designed for much coarser NWP models) assume that local, small-scale wind speed maxima responsible for gusts (which may be induced by terrain or turbulence) are unresolved and add a proportionate amount to the grid box wind in order to model potential gust strength. As these maxima start to become resolved, this assumption becomes counter-productive at their location, resulting in gusts being effectively ‘double counted’. This is an example of a ‘grey-zone’ problem. Lee waves represent a similar formerly-unresolved contribution to the local distribution of winds. It is unclear what approach should be taken for gust prediction in the presence of lee waves. The spectrum of turbulence may well be different beneath the linear, accelerated flow within a lee wave trough, as compared to the potentially weak, but turbulent flow beneath a lee wave crest, where winds, though weaker, may be more gusty. Some physically-based gust prediction methods [66] should possess a degree of sensitivity to this dichotomy, but further research is needed to know if these treatments are truly representative.

Though the model-observation comparisons in the previous section are encouraging, upper air verification of lee wave forecasts is in general limited and certainly not systematic in the same way as for basic surface meteorological variables, relying usually on occasional field campaigns involving intensive upper air and surface observations. Options do exist to potentially improve this situation, including Mesosphere-Stratosphere-Troposphere (MST) radar data [43] or high resolution data from routine radiosonde releases, but are not currently exploited. The availability of high-resolution, high-coverage in-flight measurements of atmospheric motion from ‘Mode-Selective’ (Mode-S) civil aircraft broadcasts is also on the horizon [67]. There is a more notable gap in the verification of near-surface wind impacts of lee waves. Satellite-based scatterometers tend to be of relatively low resolution and largely offer data too far from land to be useful, although the related Advanced Synthetic Aperture Radar (ASAR) technique [68], requiring an assumed wind direction inferred from NWP

data, has clear potential in coastal areas [49]. Routine station wind measurements are typically too sparse (compared to lee wave wavelengths) and too influenced by other factors to afford conclusive routine verification, and supporting information such as lee wave structure or induced pressure fluctuations [14] is absent. Nevertheless, it has been possible here, in a clear case of lee waves fairly well forecast by UKV, to use the model to attribute lee wave impacts on observed winds at surface routine observation sites. Some systematic method to isolate and quantify lee wave effects within these routine observations might be possible, perhaps by coupling with a simulated wave field and/or satellite images of wave patterns or filtering for wavelike variability across the network, offering the possibility of more routine forecast assessment.

5. Conclusions

An automated method for the diagnosis of lee wave severity and ‘risk of rotor activity’ from high resolution output fields from a linear flow model, 3DVOM, used for operational lee wave forecasting, was described. The method assumes the contribution to the perturbation of atmospheric motion over complex terrain by direct interaction with the terrain and the remote contribution by lee waves are additive. It uses the fact that both of these scale with the background wind, in order to isolate the lee wave contribution to vertical motion and to near-surface flow perturbation. Resulting diagnoses of lee wave and rotor-like activity appear to successfully convey the severity of conditions that would be gauged by eye from the inspection of maps of vertical velocity and 10-m wind and prove consistent for different cases and different U.K. mountain ranges. Note that a true, direct verification of rotor activity would require the comparison of model output with comprehensive measurements, probably involving remote sensing. In the absence of the latter, this study focusses on the magnitude of wave-induced impacts on 10-m winds, given that this is directly linked to rotor formation in the highly idealised case.

Following recent upgrades, the vertical velocities simulated by the 1.5-km resolution UKV model during lee wave cases are in good agreement with observations from recent aircraft sorties over Scotland, performing better than the 1-km resolution dry, linear 3DVOM model. UKV’s ability to simulate moist and non-linear effects (low-Froude number flows, flow separation and rotors, convection, moist stability, reversible and irreversible latent heating effects, wave interactions, etc.) and horizontal anisotropy in background conditions (e.g., convergence, cyclone structure) is likely to contribute to better forecasting of lee waves. Furthermore, lee wave impacts on near-surface winds in UKV appear to be much more consistent with those observed at synoptic monitoring sites at the time of the aircraft sorties than those forecast by 3DVOM.

Adaptation of lee wave and ‘rotor risk’ diagnostics for use with UKV will require an approach taking into account the variation of wind fields over some area (currently, the diagnostics produce a value for each of the small sub-national domains used by 3DVOM). Additionally, in UKV, these diagnostics must deal appropriately with other sources of intense vertical motion and surface wind disturbance, which 3DVOM is intrinsically unable to represent, such as convective showers and fronts. The improved simulation of lee waves and their surface wind impacts by UKV compared to 3DVOM should increase the value of these automated diagnostics. Methods for more systematic verification of lee wave forecasts and impacts would be valuable. New remote-sensing and civil aircraft-based methods offer some promise, but with research, existing routine observations could also potentially be exploited.

Acknowledgments: The authors would like to thank the FAAM ground and air staff and aircraft scientists, involved in collecting the BAe-146 data, for the crucial contribution they make to model validation and understanding of lee wave phenomena.

Author Contributions: Simon Vosper contributed text and figures concerning the results of comparisons of the UKV model with observations, Phil Brown the description of the aircraft observations and Peter Sheridan the remaining material and drafting of the manuscript. All authors contributed to the draft’s refinement before submission.

Conflicts of Interest: The authors declare no conflict of interest.

References

1. Holmboe, J.R.; Klieforth, H. *Investigation of Mountain Lee Waves and the Airflow over the Sierra Nevada*; Final Report; UCLA: Department of Meteorology, University of California, CA, USA, 1957.
2. Lilly, D.K.; Zipser, E.J. The front range windstorm of 11 January 1972—A meteorological narrative. *Weatherwise* **1972**, *25*, 56–63.
3. Durran, D.R. Another look at downslope windstorms. Part I: The development of analogs to supercritical flow in an infinitely deep, continuously stratified fluid. *J. Atmos. Sci.* **1986**, *43*, 2527–2543.
4. Jiang, Q.; Doyle, J.D. Diurnal Variation of Downslope Winds in Owens Valley during the Sierra Rotor Experiment. *Mon. Weather Rev.* **2008**, *136*, 3760–3780.
5. Peltier, W.R.; Clark, T.L. The evolution and stability of finite-amplitude mountain waves. Part II: Surface wave drag and severe downslope windstorms. *J. Atmos. Sci.* **1979**, *36*, 1498–1529.
6. Lin, Y.L.; Wang, T.A. Flow regimes and transient dynamics of two-dimensional stratified flow over an isolated mountain ridge. *J. Atmos. Sci.* **1996**, *53*, 139–158.
7. Clark, T.L.; Hall, W.D.; Kerr, R.M.; Middleton, D.; Radke, L.; Martin, F.; Neiman, P.J.; Levinson, D. Origins of aircraft-damaging clear-air turbulence during the 9 December 1992 Colorado downslope windstorm: Numerical simulations and comparison with observations. *J. Atmos. Sci.* **2000**, *57*, 1105–1131.
8. Jiang, Q.; Doyle, J.D. Gravity Wave Breaking over the Central Alps: Role of Complex Terrain. *J. Atmos. Sci.* **2004**, *61*, 2249–2266.
9. Doyle, J.D.; Shapiro, M.A.; Jiang, Q.; Bartels, D.L. Large-Amplitude Mountain Wave Breaking over Greenland. *J. Atmos. Sci.* **2005**, *62*, 3106–3126.
10. Belusic, D.; Zagar, M.; Grisogono, B. Numerical simulation of pulsations in the bora wind. *Q. J. R. Meteorol. Soc.* **2007**, *133*, 1371–1388.
11. Doyle, J.D.; Durran, D.R. The dynamics of mountain-wave-induced rotors. *J. Atmos. Sci.* **2002**, *59*, 186–201.
12. Vosper, S.B. Inversion effects on mountain lee waves. *Q. J. R. Meteorol. Soc.* **2004**, *130*, 1723–1748.
13. Vosper, S.B.; Sheridan, P.F.; Brown, A.R. Flow separation and rotor formation beneath two-dimensional trapped lee waves. *Q. J. R. Meteorol. Soc.* **2006**, *132*, 2415–2438.
14. Sheridan, P.F.; Horlacher, V.; Rooney, G.G.; Hignett, P.; Mobbs, S.D.; Vosper, S.B. Influence of lee waves on the near-surface flow downwind of the Pennines. *Q. J. R. Meteorol. Soc.* **2007**, *133*, 1353–1369.
15. Sachsperger, J.; Serafin, S.; Grubisic, V. Dynamics of rotor formation in uniformly stratified two-dimensional flow over a mountain. *Q. J. R. Meteorol. Soc.* **2016**, *142*, 1201–1212.
16. Strauss, L.; Serafin, S.; Haimov, S.; Grubisic, V. Turbulence in breaking mountain waves and atmospheric rotors estimated from airborne in situ and Doppler radar measurements. *Q. J. R. Meteorol. Soc.* **2015**, *141*, 3207–3225.
17. Strauss, L.; Serafin, S.; Grubisic, V. Atmospheric Rotors and Severe Turbulence in a Long Deep Valley. *J. Atmos. Sci.* **2016**, *73*, 1481–1506.
18. Hertenstein, R.F.; Kuettner, J. Rotor types associated with steep lee topography: Influence of the wind profile. *Tellus A* **2005**, *57*, 117–135.
19. Grisogono, B.; Belusic, D. A review of recent advances in understanding the meso- and micro-scale properties of the severe Bora wind. *Tellus A* **2009**, *61*, 1–16.
20. Agustsson, H.; Olafsson, H. Mean gust factors in complex terrain. *Meteorol. Z.* **2004**, *13*, 149–155.
21. Scorer, R.S. Theory of waves in the lee of mountains. *Q. J. R. Meteorol. Soc.* **1949**, *75*, 41–56.
22. Shutts, G.J. Operational lee wave forecasting. *Meteorol. Appl.* **1997**, *4*, 23–35.
23. Doyle, J.D.; Durran, D.R. Recent developments in the theory of atmospheric rotors. *Bull. Am. Meteorol. Soc.* **2004**, *85*, 337–342.
24. Doyle, J.D.; Durran, D.R. Rotor and subrotor dynamics in the lee of three-dimensional terrain. *J. Atmos. Sci.* **2007**, *64*, 4202–4221.
25. Doyle, J.D.; Grubisic, V.; Brown, W.O.J.; Wekker, S.F.J.D.; Doernbrack, A.; Jiang, Q.; Mayor, S.D.; Weissmann, M. Observations and numerical simulations of subrotor vortices during T-REX. *J. Atmos. Sci.* **2009**, *66*, 1224–1249.
26. Knigge, C.; Etling, D.; Pacib, A.; Eiff, O. Laboratory experiments on mountain-induced rotors. *Q. J. R. Meteorol. Soc.* **2010**, *136*, 442–450.

27. Teixeira, M. Diagnosing Lee Wave Rotor Onset Using a Linear Model Including a Boundary Layer. *Atmosphere* **2017**, *8*, 5.
28. Mobbs, S.D.; Vosper, S.B.; Sheridan, P.F.; Cardoso, R.; Burton, R.R.; Arnold, S.J.; Hill, M.K.; Horlacher, V.; Gadian, A.M. Observations of downslope winds and rotors in the Falkland Islands. *Q. J. R. Meteorol. Soc.* **2005**, *131*, 329–351.
29. Sheridan, P.F.; Vosper, S.B. A flow regime diagram for forecasting lee waves, rotors and downslope winds. *Meteorol. Appl.* **2006**, *13*, 179–195.
30. Sheridan, P.F.; Vosper, S.B. Numerical simulations of rotors, hydraulic jumps and eddy shedding in the Falkland Islands. *Atmos. Sci. Lett.* **2006**, *6*, 211–218.
31. Mayr, G.J.; Armi, L. The Influence of Downstream Diurnal Heating on the Descent of Flow across the Sierras. *J. Appl. Meteorol. Climatol.* **2010**, *49*, 1906–1912.
32. Webster, S.; Brown, A.R.; Cameron, D.R.; Jones, C.P. Improvements to the representation of orography in the Met Office Unified Model. *Q. J. R. Meteorol. Soc.* **2003**, *129*, 1989–2010.
33. Turner, J. *Development of a Mountain Wave Turbulence Prediction Scheme for Civil Aviation*; Forecasting Research Technical Report No. 265; Met Office: Exeter, UK, 1999.
34. Sharman, R.; Tebaldi, C.; Wiener, G.; Wolff, J. An integrated approach to mid- and upper-level turbulence forecasting. *Weather Forecast.* **2006**, *21*, 268–287.
35. Gill, P.G. Objective verification of World Area Forecast Centre clear air turbulence forecasts. *Meteorol. Appl.* **2014**, *21*, 3–11.
36. Teixeira, M.; Argain, J.L.; Miranda, P.M.A. Orographic Drag Associated with Lee Waves Trapped at an Inversion. *J. Atmos. Sci.* **2013**, *20*, 2930–2947.
37. Wong, W.K.; Lau, C.S.; Chan, P.W. Aviation model: A fine-scale numerical weather prediction system for aviation applications at the Hong Kong International Airport. *Adv. Meteorol.* **2013**, *2013*, 532475.
38. Chan, P.W.; Hon, K.K. Performance of super high resolution numerical weather prediction model in forecasting terrain-disrupted airflow at the Hong Kong International Airport: Case studies. *Meteorol. Appl.* **2016**, *23*, 101–114.
39. Li, L.; Chan, P.W. Numerical simulation study of the effect of buildings and complex terrain on the low-level winds at an airport in typhoon situation. *Meteorol. Z.* **2012**, *21*, 183–192.
40. Carruthers, D.; Ellis, A.; Chan, J.H.P.W. Modelling of wind shear downwind of mountain ridges at Hong Kong International Airport. *Meteorol. Appl.* **2014**, *21*, 94–104.
41. Rasheed, A.; Suld, J.K.; Kvamsdala, T. A Multiscale Wind and Power Forecast System for Wind Farms. *Energy Procedia* **2014**, *53*, 290–299.
42. Vosper, S.B. Development and testing of a high resolution mountain-wave forecasting system. *Meteorol. Appl.* **2003**, *10*, 75–86.
43. Vosper, S.B.; Worthington, R.M. VHF radar measurements and model simulations of mountain waves over Wales. *Q. J. R. Meteorol. Soc.* **2002**, *128*, 185–204.
44. Vosper, S.B.; Wells, H.; Sinclair, J.A.; Sheridan, P.F. A climatology of lee waves over the UK derived from model forecasts. *Meteorol. Appl.* **2013**, *20*, 466–481.
45. Grubisic, V.; Doyle, J.D.; Kuettner, J.; Mobbs, S.; Smith, R.B.; Whiteman, C.D.; Dirks, R.; Czyzyk, S.; Cohn, S.A.; Vosper, S.; et al. The Terrain-Induced Rotor Experiment: A field campaign overview including observational highlights. *Bull. Am. Meteor. Soc.* **2008**, *89*, 1513–1533.
46. Casswell, S.A. A simplified calculation of maximum vertical velocities in mountain lee waves. *Meteorol. Mag.* **1966**, *95*, 68–80.
47. Agustsson, H.; Olafsson, H. Simulating a severe windstorm in complex terrain. *Meteorol. Z.* **2007**, *16*, 111–122.
48. Agustsson, H.; Olafsson, H. The bimodal downslope windstorms at Kvisker. *Meteorol. Atmos. Phys.* **2012**, *116*, 27–42.
49. Agustsson, H.; Olafsson, H. Simulations of observed lee waves and rotor turbulence. *Mon. Weather Rev.* **2014**, *142*, 832–849.
50. Tang, Y.; Lean, H.W.; Bornemann, J. The benefits of the Met Office variable resolution NWP model for forecasting convection. *Meteorol. Appl.* **2013**, *20*, 417–426.
51. Wood, N.; Staniforth, A.; White, A.; Allen, T.; Diamantakis, M.; Gross, M.; Melvin, T.; Smith, C.; Vosper, S.; Zerroukat, M.; et al. An inherently mass-conserving semi-implicit semi-Lagrangian discretisation of the deep-atmosphere global nonhydrostatic equations. *Q. J. R. Meteorol. Soc.* **2014**, *140*, 1505–1520.

52. Sheridan, P.F.; Vosper, S.B. High-resolution simulations of lee waves and downslope winds over the Sierra Nevada during T-REX IOP 6. *J. Appl. Meteorol. Climatol.* **2012**, *51*, 1333–1352.
53. Doyle, J.D.; Gaberseck, S.; Jiang, Q.; Bernardet, L.; Brown, J.M.; Dornbrack, A.; Filause, E.; Grubisic, V.; Kirshbaum, D.J.; Knoth, O.; et al. Mountain-Wave Simulations and Implications for Mesoscale Predictability. *Mon. Weather Rev.* **2011**, *139*, 2811–2831.
54. Renfrew, I.A.; Outten, S.D.; Moore, G.W.K. An easterly tip jet off Cape Farewell, Greenland. I: Aircraft observations. *Q. J. R. Meteorol. Soc.* **2009**, *135*, 1919–1933.
55. Petersen, G.N.; Renfrew, I.A. Aircraft-based observations of air-sea fluxes over Denmark Strait and the Irminger Sea during high wind speed conditions. *Q. J. R. Meteorol. Soc.* **2009**, *135*, 2030–2045.
56. Beswick, K.M.; Gallagher, M.W.; Webb, A.R.; Norton, E.G.; Perry, F. Application of the Aventech AIMMS20AQ airborne probe for turbulence measurements during the Convective Storm Initiation Project. *Atmos. Chem. Phys.* **2008**, *8*, 5449–5463.
57. Khelif, D.; Burns, S.P.; Friehe, C.A. Improved wind measurements on research aircraft. *J. Atmos. Ocean. Technol.* **1999**, *16*, 860–875.
58. Jiang, Q. Moist dynamics and orographic precipitation. *Tellus A* **2003**, *55*, 301–316.
59. Doyle, J.D.; Smith, R.B. Mountain waves over the Hohe Tauern: Influence of upstream diabatic effects. *Q. J. R. Meteorol. Soc.* **2003**, *129*, 799–823.
60. Jiang, Q.; Doyle, J.D. The Impact of Moisture on Mountain Waves during T-REX. *Mon. Weather Rev.* **2009**, *137*, 3888–3906.
61. Worthington, R.M. Radar measurement of the effect of boundary-layer saturation on mountain-wave amplitude. *Meteorol. Atmos. Phys.* **2009**, *105*, 29–35.
62. Rognvaldsson, O.; Bao, J.W.; Agustsson, H.; Olafsson, H. Downslope windstorm in Iceland—WRF/MM5 model comparison. *Atmos. Chem. Phys.* **2011**, *11*, 103–120.
63. Smith, R.B.; Jiang, Q.; Doyle, J.D. A theory of gravity wave absorption by boundary layers. *J. Atmos. Sci.* **2006**, *63*, 774–781.
64. Jiang, Q.; Smith, R.B.; Doyle, J.D. Interaction between trapped waves and boundary layers. *J. Atmos. Sci.* **2006**, *63*, 617–633.
65. Smith, R.B. Interacting Mountain Waves and Boundary Layers. *J. Atmos. Sci.* **2007**, *64*, 594–607.
66. Sheridan, P. *Review of Techniques and Research for Gust Forecasting and Parameterisation*; Forecasting Research Technical Report No. 570; Met Office: Exeter, UK, 2011.
67. Mirza, A.K.; Ballard, S.P.; Dance, S.L.; Maisey, P.; Rooney, G.G.; Stone, E.K. Comparison of aircraft derived observations with in situ research aircraft measurements. *Q. J. R. Meteorol. Soc.* **2016**, *142*, 2949–2967.
68. Furevik, B.R.; Schyberg, H.; Noer, G.; Tveter, F.; Roehrs, J. ASAR and ASCAT in Polar Low Situations. *J. Atmos. Ocean. Technol.* **2015**, *32*, 783–792.

